Chemical long-range disorder in Prussian blue analogues for potassium storage

Chongwei Gao,[1] Jiantao Li,[2] Tian Sun,[3] Ming Chen,[3] Xunan Wang,[1] Guobin Zhang,[4] Shuhua Zhang,[1] Sungsik Lee,[5] Tianyi Li,[5] Khalil Amine,[2] Guang Feng,[3] Dengyun Zhai,[1]* and Feiyu Kang[1]**

[1]Shenzhen Geim Graphene Center, Institute of Materials Research, Tsinghua Shenzhen International Graduate School, Tsinghua University, Shenzhen 518055, China.

[2]Chemical Sciences and Engineering Division, Argonne National Laboratory, Lemont, IL 60439, USA.

[3]State Key Laboratory of Coal Combustion and School of Energy and Power Engineering, Huazhong University of Science and Technology, Wuhan 430070, China.

[4]Future Technology School, Shenzhen Technology University, Shenzhen 518118, China.

[5]X-ray Science Division, Advanced Photon Source, Argonne National Laboratory, Lemont, Illinois 60439, United States.

AUTHOR INFORMATION

Corresponding Author

Feiyu Kang: fykang@sz.tsinghua.edu.cn; fykang@mail.tsinghua.edu.cn

Dengyun Zhai: zhaidy0404@sz.tsinghua.edu.cn

Jiantao Li: jiantao.li@anl.gov; jiantao_work@126.com

Abstract: Ordered Prussian Blue Analogues (PBAs) are vital cathode materials for ion storage, but strong interactions between the framework and host ions, especially large ions like K^+, hinder ion migration, leading to poor diffusion kinetics and reduced reaction activity. Here, we present an approach to overcome this challenge by constructing chemical long-range disorder (LRD) in PBAs, involving maintaining inherent local coordination while introducing disorder over long-range spatial dimensions. Order control is achieved by introducing a large-sized lattice to disrupt the original lattice growth during synthesis. Unlike traditional monocrystalline particles, the abundant grain boundaries in the obtained LRD structure create significant potential fluctuations, generating additional electric fields that enhance ion transport. Furthermore, the short lattice coherence length reduces interaction between the framework and K^+. These factors collectively contribute to the improved electrochemical activity of LRD PBAs during K^+ storage. This finding opens new avenues for designing PBA structures and offers insights into their structure-electrochemical performance relationship.

TOC GRAPHICS

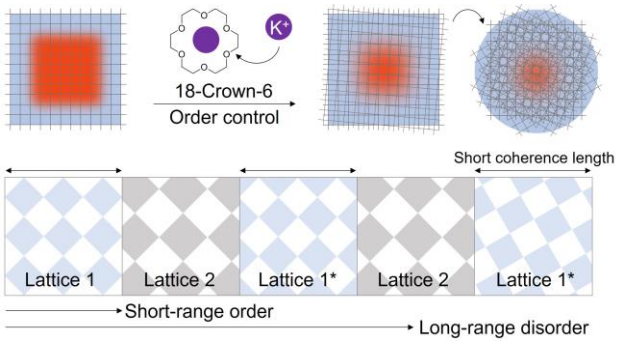

PBAs are promising host materials for storing various ions, including Li^+, Na^+, K^+, and Zn^{2+}, making them significant electrode materials.[1-9] Their low-cost and straightforward synthesis methods provide substantial potential for future commercialization. However, PBAs interact strongly with host ions, particularly larger and highly charged ions, hindering ion transport.[3, 10, 11] For instance, compared to Na^+, the diffusion depth of larger K^+ in PBAs is extremely limited, and their electrochemical activity significantly decreases as grain size increases.[10] Despite employing various strategies such as ion doping[1, 2, 12] to achieve stable potassium storage performance in PBAs, challenges remain unresolved regarding reaction depth.

Order control has become a recent research focus, particularly in layered transition-metal oxides.[13-15] Compared to well-ordered phases, partially disordered phases have been demonstrated to effectively improve Li^+ diffusivity and increase capacity.[14] It is suggested that a short coherence length of spinel-like environments in cation-disordered rocksalts (DRXs) helps mitigate detrimental phase transitions and potentially enhances rate performance.[14] Order control has also been applied to other materials, including some anode materials,[16-19] demonstrating a notable strategy to improve rate capability.

In this work, we showcase the application of order control in Mn-based PBAs (MnHCF) to overcome poor kinetics and capacity degradation during K^+ storage. The coherence length of the K^+-rich contracted lattice was regulated by introducing a K^+-deficient expanded lattice, resulting in long-range disordered MnHCF. In this structure, the local coordination environment of redox-active Fe/Mn remains unchanged, as confirmed by X-ray Absorption Spectroscopy (XAS), ensuring the storage progress. The grain boundaries between sub-lattices were found to alter the local electrostatic potential, thereby inducing additional electric fields that facilitate K^+ transport, as confirmed by Atomic Force Microscopy-Kelvin Probe Force Microscopy (AFM-KPFM) and

Galvanostatic Intermittent Titration Technique (GITT). This strategy significantly enhances the reaction depth for K^+ and ensures excellent cycling stability. The long-range disorder approach presents novel opportunities for enhancing the performance of PBAs.

To reduce the coherence length of the original lattice of PBAs, additional interfering lattices can be introduced. The introduced lattices should have comparable compositions and closely matched atomic arrangements to ensure chemical compatibility. Here, we utilized the contraction effect of alkali metal ions to achieve two different-sized lattices, meeting the above goal.

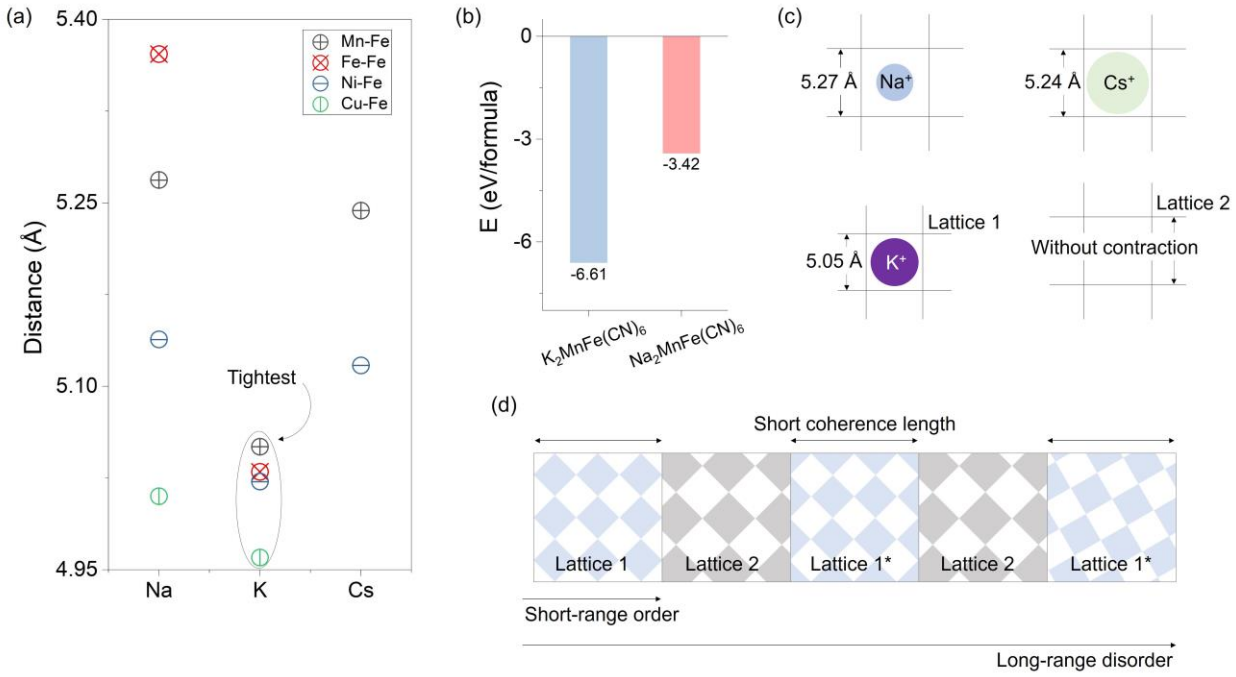

Figure 1. Screening the composition for LRD design. (a) Average TM-Fe distance in $A_2TMFe(CN)_6$. TM is the transition metal element and A is the alkali metal element. (b) Calculated formation energy of $K_2MnFe(CN)_6$ and $Na_2MnFe(CN)_6$ by DFT. (c) Average Mn-Fe distance of A^+-containing MnHCF and A^+-free MnHCF, where A includes Na^+, K^+, and Cs^+. (d) The concept of constructed LRD structure in PBAs.

By searching the inorganic crystal structure database, the existing $A_2TMFe(CN)_6$ structures (where A indicates $Na^+/K^+/Cs^+$, and TM indicates Mn/Fe/Ni/Cu) and corresponding X-ray Diffraction (XRD) patterns are shown in **Figures S1-S4**. The average distances of TM-Fe, which present the size of the lattice's subcube, are shown in **Figure 1a**. It was observed that the subcube size is not directly correlated with the radius of the embedded A^+. Among them, K^+, which has a medium ionic radius, causes the tightest lattice contraction in PBAs. This difference is the result of multiple factors, including the site occupancy of alkali metal ions and their interactions with the lattice[3]. The formation energies of $K_2MnFe(CN)_6$ and $Na_2MnFe(CN)_6$ were calculated using density functional theory (DFT). As shown in **Figure 1b**, the calculated formation energy of $K_2MnFe(CN)_6$ is -6.61 eV/formula much lower than that of $Na_2MnFe(CN)_6$ at -3.42 eV/formula. This suggests that the interaction between K^+ and the framework structure is stronger, leading to a more pronounced contraction. As a result, the average Mn-Fe distance in the K^+-containing MnHCF lattice (termed Lattice 1) is around 5.05 Å, significantly shorter than that in the Na^+-containing (5.27 Å) and Cs^+-containing (5.24 Å) lattices (**Figure 1c**).

On this basis, K^+-containing MnHCF was screened for LRD design. A^+-free MnHCF (termed Lattice 2) can be partially introduced into the structure to reduce the coherence length of Lattice 1. This interference can cause orientation differences between adjacent Lattice 1 regions, forming sub-grains and ultimately achieving an LRD structure (**Figure 1d**).

To implement the above strategy, we initially synthesized a continuous K^+-containing MnHCF (termed as Mn[Fe]) for comparison. Ethylenediaminetetraacetic acid dipotassium salt (EDTA-2K), known to significantly reduce reaction rates, was utilized to construct a nearly perfect Lattice 1.[20] Subsequently, 18-Crown-6, known for its specific combination with K^+, was employed to restrict K^+ and partially form Lattice 2 during the synthesis of Mn[Fe], achieving the desired LRD

structure (termed as Mn[Fe]-LRD) (**Figure 2a**). By adjusting the concentration of 18-Crown-6, the coherence length can be further controlled.

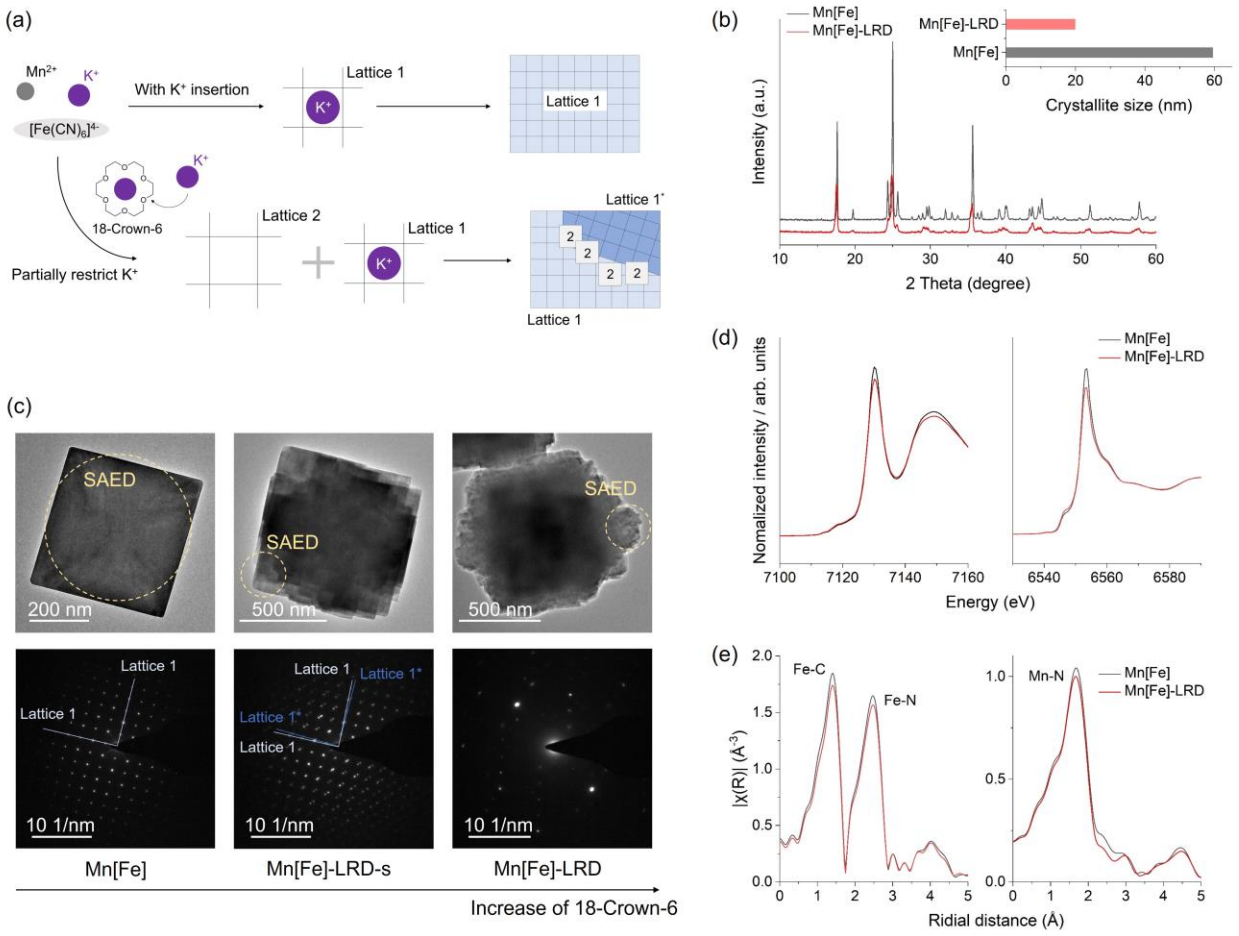

Figure 2. LRD construction and structural characterizations. (a) Schematic diagram of the synthesis. (b) XRD patterns of Mn[Fe] and Mn[Fe]-LRD. (c) TEM images and corresponding SAED patterns of Mn[Fe], Mn[Fe]-LRD-s, and Mn[Fe]-LRD. (d) XANES spectra at the Fe K-edge (left) and Mn K-edge (right) for Mn[Fe] and Mn[Fe]-LRD. (e) EXAFS spectra at the Fe K-edge (left) and Mn K-edge (right) for Mn[Fe] and Mn[Fe]-LRD.

The XRD patterns of as-synthesized materials are shown in **Figure 2b**. Despite identical peak positions, the crystallinity differs significantly. The Full Width at Half Maximum (FWHM) at 25°

for Mn[Fe]-LRD is 0.410, much larger than 0.137 for Mn[Fe], corresponding to a crystallite size of around 20 nm calculated by the Scherrer formula. Rietveld refinement based on high-energy XRD measurement indicates a monoclinic structure ($P2_1/c$ symmetry), consistent with the previous report (**Figure S4**).[21] The atomic ratios were confirmed by inductively coupled plasma-atomic emission spectrometry (ICP) tests (**Table S1**), and the refined structural parameters were listed in **Table S2**.

The Transmission Electron Microscopy (TEM) and Scanning Electron Microscopy (SEM) images of obtained samples are shown in **Figure 2c** and **S5**. Mn[Fe] has a cubic shape with a particle size of around 500 nm. The Selected Area Electron Diffraction (SAED) patterns of Mn[Fe] indicate a monocrystalline structure. More SAED patterns along different crystal zone axes of the same particle are shown in **Figure S6**. All the SAED patterns come from the same lattice arrangement. When a moderate concentration of 18-Crown-6 was added, the obtained sample (termed as Mn[Fe]-LRD-s) showed jagged particle edges and a slight increase in particle size (**Figure 2c** and **S5**). At least two lattices at a certain growth orientation (marked as lattice 1 and lattice 1^*) were observed at the corner of the particle according to the SAED patterns. More SAED patterns of Mn[Fe]-LRD-s are shown in **Figure S7**. Compared to Mn[Fe], the SAED pattern comes from the whole particle becoming diffuse, indicating a decrease in lattice coherence length (**Figure S7b**). The elongated SAED patterns along different edges demonstrate preferential growth orientations of different lattices within the particle (**Figure S7c and d**), supporting our hypothesis. After increasing the concentration of 18-crown-6 during the synthesis, the resultant Mn[Fe]-LRD sample exhibits a more obvious disordered structure. As shown in **Figure 2c** and **S5** the morphology is further changed from cubic to spheroidal with more jagged edges. The distribution of SAED patterns of Mn[Fe]-LRD becomes disordered (**Figure 2c**). As shown in **Figure S8**,

Mn[Fe] exhibits long-range ordered atomic arrangement, while Mn[Fe]-LRD has indistinct lattice fringes due to lattice stacking.

X-ray absorption near-edge spectroscopy (XANES) was used to determine the oxidation states of Fe and Mn. As shown in **Figure 2d**, the white lines in Fe and Mn K-edge XANES spectra, corresponding to 1s→4p transition, are located at 7130 eV and 6553 eV, indicating Fe^{2+} and Mn^{2+} in both Mn[Fe] and Mn[Fe]-LRD samples.[20, 22] Fourier transformed extended X-ray absorption fine structure (EXAFS) spectra confirm that the local coordinated environments of TMs maintain the same in Mn[Fe] and Mn[Fe]-LRD (**Figure 2e**), consistent with the previous reports.[23] Fourier-Transform Infrared (FT-IR) spectra further confirm the similar chemical environments (**Figure S9**). All absorption peaks remain consistent across the three samples. Thus, the addition of 18-Crown-6 only alters the long-range order of the obtained samples, while the local coordination environments remain unchanged.

To further demonstrate the role of 18-Crown-6 in building LRD structures, different types of crown ethers were used for synthesis (**Figure S10a**). It's known that 18-Crown-6 has the specific selectivity with K^+ to form a stable complex. The stable constant (Log K) can reach 2.03 in an aqueous solution at 25 ℃ because the diameter of K^+ (2.7 Å) can match well with the size of 18-Crown-6 (2.6-3.2 Å).[24, 25] In contrast, 15-Crown-5 has a smaller ring size (1.7-2.2 Å) and thus shows a weak combination with K^+ (log K=0.74).[24] The resultant sample (named Mn[Fe]_15-Crown-5) has a similar XRD pattern as Mn[Fe], and the FWHM remains 0.188 at 25°, indicating a similar structure (**Figure S10b**). The corresponding SEM image is shown in **Figure S10c**. The particles of Mn[Fe]_15-Crown-5 remain cubic as Mn[Fe]. Thus, the control of K^+ release is the primary reason for the generation of LRD structure. Benzo-18-Crown-6, owning the same hole size as 18-Crown-6 (**Figure S10a**), was used to further verify the above conclusion. Although the

solubility of Benzo-18-Crown-6 decreases due to the introduction of the benzene ring, the resultant sample (named Mn[Fe]_Benzo-18-Crown-6) shows a similar XRD pattern and spherical particle shape as Mn[Fe]-LRD (**Figure S10b** and **S10d**). The corresponding FWHM of the peak at 25° increases to 0.275, indicating an LRD structure. All results confirm that order control in MnHCF can be achieved by regulating K^+ insertion.

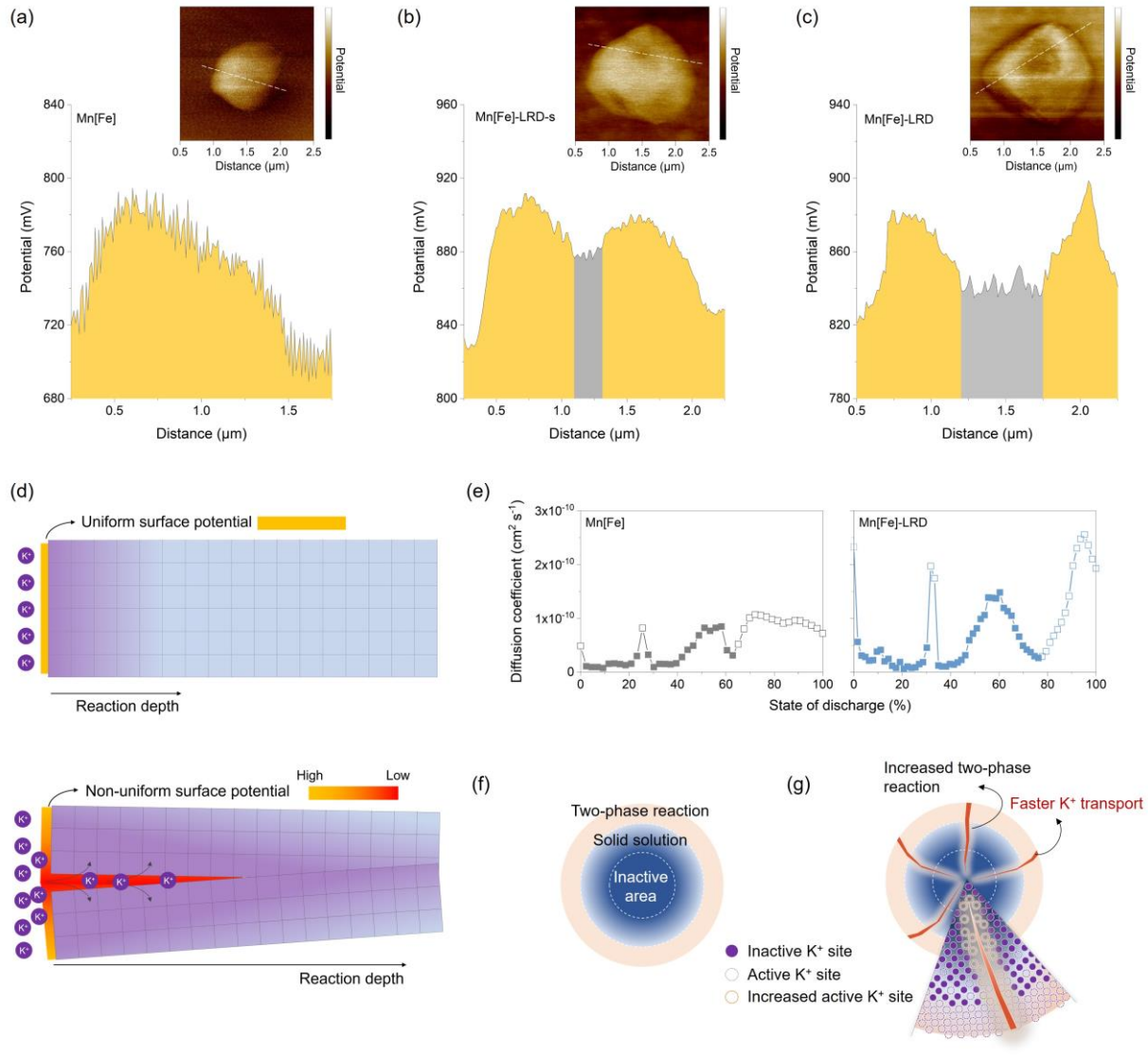

Figure 3. Potential distribution difference and reaction depth analysis. (a-c) Surface potential profiles along the line in AFM-KPFM images of Mn[Fe], Mn[Fe]-LRD-s, and Mn[Fe]-LRD, respectively. (d) Schematic of the additional electric field. (e) GITT test results for Mn[Fe] and

Mn[Fe]-LRD. Schematic illustrations of (f) Mn[Fe] and (g) Mn[Fe]-LRD showing different reaction depths.

By the order control, the obtained samples exhibit significant differences in potential distribution (**Figure 3a-c**). This phenomenon can be attributed to compositional and structural fluctuations at grain boundaries, resulting in non-uniform charge distribution. AFM-KPFM observations show that Mn[Fe] has a relatively uniform surface potential without significant fluctuations (**Figure 3a**). However, as long-range order decreases, notable surface potential variations emerge (**Figures 3b** and **3c**). These potential differences generate additional electric fields, favoring K^+ transport (**Figure 3d**). GITT results confirm it (**Figure 3e**). The K^+ diffusion coefficient (D) was evaluated during the discharging process. The calculated D value of K^+ in Mn[Fe]-LRD is much higher than that in Mn[Fe] during the whole discharging process.

Additionally, the improved K^+ transport ability also improves the reaction depth. The solid and hollow points in **Figure 3e** represent the two-phase and solid solution regions, respectively.[11] For low-activity PBAs, the solid solution regions are typically inside the particles (**Figure 3f**). In these areas, limited ion transport results in only partial ion insertion/extraction, which does not alter the crystal phase. The higher proportion of two-phase regions in Mn[Fe]-LRD indicates a greater number of active K^+ sites within the particles (**Figure 3g**).

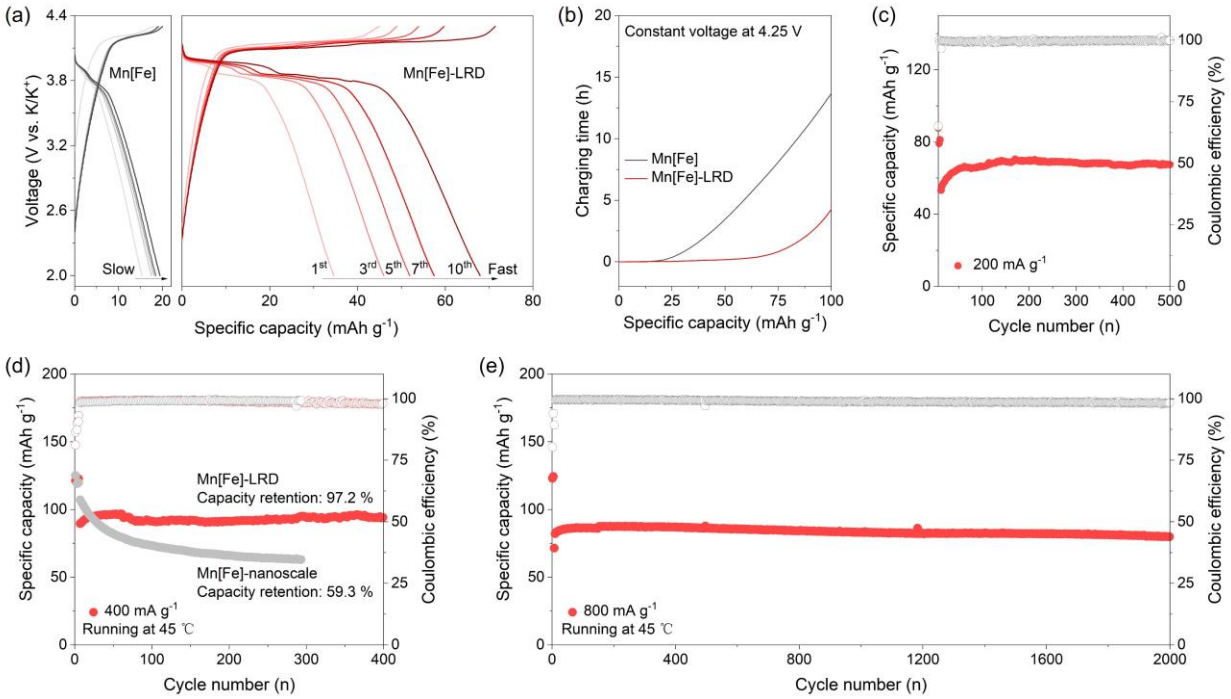

Figure 4. Electrochemical performance comparison. (a) Galvanostatic charge-discharge voltage profiles of Mn[Fe] and Mn[Fe]-LRD for the first ten cycles at 50 mA g^{-1}. (b) Comparisons of the charging time at a constant voltage of 4.25 V. (c) Cyclic performance of Mn[Fe]-LRD at 200 mA g^{-1} at 25 ℃. (d) Cyclic performance comparison between Mn[Fe]-nanoscale and Mn[Fe]-LRD at 400 mA g^{-1} at 45 ℃. (e) Long-term cyclic performance of Mn[Fe]-LRD at 800 mA g^{-1} at 45 ℃. This cell was assembled by using K@carbon fibers as the anode to optimize the electrochemical behavior of the anode side. All Mn[Fe]-LRD cells were activated at a current of 50 mA g^{-1} for the first five cycles, followed by potentiostatic charging in the 6th cycle.

The electrochemical performance was further evaluated. Mn[Fe] with a big particle size has low electrochemical reactivity for K^+ storage, which is a common issue as reported[10]. As shown in **Figure 4a**, even at a low current density of 50 mA g^{-1}, the initial specific capacity of Mn[Fe] was

only 15.3 mAh g^{-1} and slowly increased to 19.5 mAh g^{-1} at the 10th cycle. This low capacity is primarily due to the strong interaction between K^+ and the frame structure.

In contrast, Mn[Fe]-LRD showed significantly improved reaction activity, even with a larger particle size of around 1 μm. Mn[Fe]-LRD displayed a rapid capacity increase from 34.5 to 67.9 mAh g^{-1} over the first 10 cycles (**Figure 4a**). We compared the de-potassium processes of the two materials under potentiostatic charging at 4.25 V (**Figure 4b**). When the charging capacity reached 20 mAh g^{-1}, Mn[Fe] exhibited sluggish reaction kinetics, resulting in significantly increased required charging time. In contrast, Mn[Fe]-LRD showed a much stronger de-potassium capability, indicating a decreased interaction between the framework structure and K^+ with a short lattice coherence length. The difference in reaction kinetics was further validated through the cyclic voltammetry (CV) tests (**Figure S11**). Mn[Fe] lost its current response at 0.3 mV/s (**Figure S11a**). Conversely, Mn[Fe]-LRD exhibited increasing current response at higher scan rates, with stable redox peak positions (**Figure S11b**), indicating enhanced reaction kinetics and excellent electrochemical reversibility. In addition, Mn[Fe]-LRD showed significantly lower electrochemical polarization (0.17 V) compared to Mn[Fe] (0.34 V) at 0.1 mV/s (**Figure S11c**).

Furthermore, *in-situ* EIS was conducted during the first four cycles (**Figure S12a and b**). Two adjacent semicircles at high frequency can be observed in the corresponding Nyquist plots, as shown in **Figure S12c and d**. The distribution of relaxation times (DRT) analysis was used to decouple the electrochemical processes (**Figure S12e**).[26, 27] The peak in the range of 10^{-2} to 10^{-1} s can be attributed to charge transfer impedance (R_{ct}), which represents a sluggish process delivering the smallest time constant in DRT plots.[27] Although the R_{ct} decreased for both materials with cycling, the R_{ct} of Mn[Fe]-LRD remained significantly lower than that of Mn[Fe], indicating better interfacial electrode reactions.

After the potentiostatic charging, Mn[Fe]-LRD can achieve a reversible capacity of 85 mAh g^{-1}, much higher than 54 mAh g^{-1} for Mn[Fe] (**Figure S13a**). The rate performance is shown in **Figure S13b**, Mn[Fe]-LRD demonstrates a better rate ability with a capacity of 42.2 mAh g^{-1} at 500 mA g^{-1}. Mn[Fe]-LRD also exhibits excellent cyclic stability, realizing more than 500 cycles without any capacity degradation at 200 mA g^{-1} (**Figure 4c**).

The high-temperature cyclic performance was also evaluated. As shown in **Figure 4d**, Mn[Fe]-LRD exhibited a capacity of around 90 mAh g^{-1} at 400 mA g^{-1} at 45 ℃. The cyclic performance of nanometer-sized MnHCF (around 30 nm, named Mn[Fe]-nanoscale) has also been tested. The corresponding XRD patterns and SEM images are shown in **Figure S14**. Mn[Fe]-nanoscale exhibited a higher initial capacity, benefiting from the small particle size, but experienced serious capacity degradation with a capacity retention of only 59.8 % after 250 cycles. In contrast, Mn[Fe]-LRD displayed superior cyclic stability. The capacity retention remained 97.2 % after 400 cycles. *In-situ* XRD demonstrated the high structural reversibility of Mn[Fe]-LRD, revealing a reversible phase transition from Monoclinic to Cubic to Tetragonal during charging and the reverse during discharging (**Figure S15**).[1] The cyclic performance of Mn[Fe]-LRD at 45 ℃ was evaluated in a more stable system using K@carbon fibers as the anode (**Figure 4e**). Eventually, the cell of Mn[Fe]-LRD|K@carbon fibers realized more than 2000 cycles without any capacity degradation. The reversible capacity reached 87 mAh g^{-1} even at a high current density of 800 mA g^{-1}.

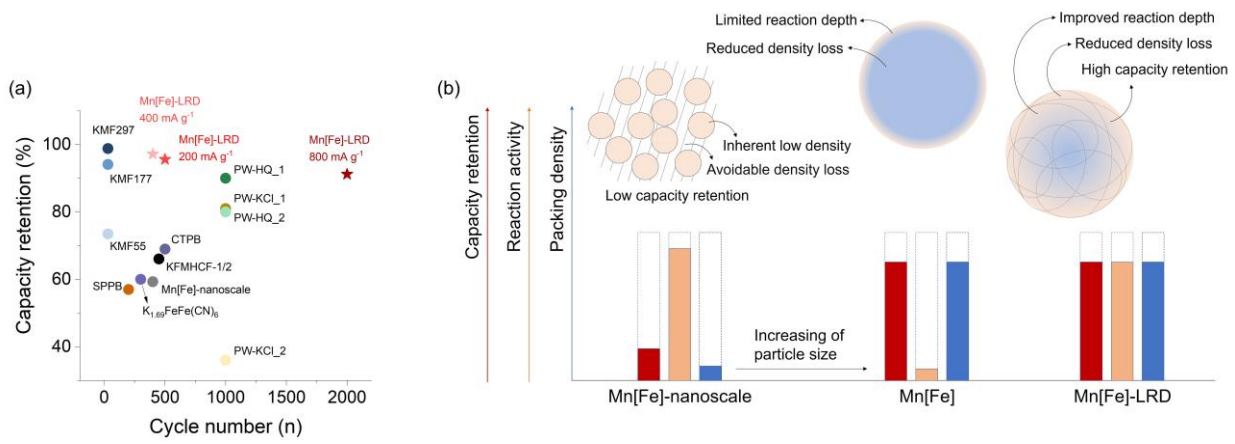

Figure 5. (a) Performance comparison with reported PBAs as PIBs cathodes. (b) The advantages of constructing LRD PBAs materials.

Comparison of this work with reported PBAs cathodes for PIBs demonstrates the remarkable cyclic stability of Mn[Fe]-LRD, highlighting its potential as a superior cathode material for K^+ storage (**Figure 5a** and **Table S3**). The electrochemical results indicate that order control can overcome the size constraints of PBAs for K^+ storage. It enables large-sized PBAs to achieve high capacity with stable cyclic performance, alleviating the stacking density loss and poor cyclic performance of small-sized PBAs (**Figure 5b**). This advancement paves the way for the development of high-energy batteries using PBAs in the future.

In summary, we demonstrate that the strategy of chemical long-range disorder significantly enhances the reaction depth of PBAs. The prepared Mn[Fe]-LRD exhibits excellent cycling stability and reaction activity comparable to nanosized Mn[Fe], overcoming the long-standing size constraint of PBAs for K^+ storage. This improvement is attributed to the additional electric fields induced by grain boundaries and the weakened interaction between the framework structure and K^+, due to the short lattice coherence length. We believe that this strategy can also be effective for

enhancing the electrochemical behavior of multi-charge ion storage and shows promise for application in other PBAs in the future.

ASSOCIATED CONTENT

Supporting Information. Experimental methods: synthesis methods of materials, structural characterization methods, electrochemical characterization methods, and theoretical calculation methods. Related figures include crystal structures, high-energy XRD patterns, SEM/TEM images, FT-IR spectra, XRD patterns, electrochemical performance, and additional tables.

AUTHOR INFORMATION

Corresponding Authors

Feiyu Kang: fykang@sz.tsinghua.edu.cn; fykang@mail.tsinghua.edu.cn

Dengyun Zhai: zhaidy0404@sz.tsinghua.edu.cn

Jiantao Li: jiantao.li@anl.gov; jiantao_work@126.com

Notes

The authors declare no competing financial interest.

ACKNOWLEDGMENT

This work is financially supported by the National Natural Science Foundation of China (No. 52072206 and No. 52361165621), National Key R&D Program of China (2021YFA1202802), Shenzhen Outstanding Talents Training Fund, and Shenzhen Technical Plan Project (No. JCYJ20220818101003008). This work gratefully acknowledges support from the U.S. Department of Energy (DOE), Office of Energy Efficiency and Renewable Energy, Vehicle Technologies Office. This research used resources of the Advanced Photon Source, a U.S. Department of Energy

(DOE) Office of Science User Facility (beamlines 12-BM and 11-ID-C), operated for the DOE Office of Science by Argonne National Laboratory under Contract No. DE-AC02- 06CH11357.

REFERENCES

(1) Jiang, L. W.; Lu, Y. X.; Zhao, C. L.; Liu, L. L.; Zhang, J. N.; Zhang, Q. Q.; Shen, X.; Zhao, J. M.; Yu, X. Q.; Li, H.; Huang, X. J.; Chen, L. Q.; Hu, Y. S., Building aqueous K-ion batteries for energy storage. *Nat. Energy* **2019**, *4*, 495-503.

(2) Ge, J. M.; Fan, L.; Rao, A. M.; Zhou, J.; Lu, B. G., Surface-substituted Prussian blue analogue cathode for sustainable potassium-ion batteries. *Nat. Sustain.* **2022**, *5*, 225-234.

(3) Hurlbutt, K.; Wheeler, S.; Capone, I.; Pasta, M., Prussian blue analogs as battery materials. *Joule* **2018**, *2*, 1950-1960.

(4) Wang, L.; Song, J.; Qiao, R.; Wray, L. A.; Hossain, M. A.; Chuang, Y. D.; Yang, W.; Lu, Y.; Evans, D.; Lee, J. J.; Vail, S.; Zhao, X.; Nishijima, M.; Kakimoto, S.; Goodenough, J. B., Rhombohedral Prussian white as cathode for rechargeable sodium ion batteries. *J. Am. Chem. Soc.* **2015**, *137*, 2548-2554.

(5) You, Y.; Wu, X. L.; Yin, Y. X.; Guo, Y. G., High-quality Prussian blue crystals as superior cathode materials for room-temperature sodium-ion batteries. *Energ. Environ. Sci.* **2014**, *7*, 1643-1647.

(6) Zhang, Z.; Avdeev, M.; Chen, H.; Yin, W.; Kan, W. H.; He, G., Lithiated Prussian blue analogues as positive electrode active materials for stable non-aqueous lithium-ion batteries. *Nat. Commun.* **2022**, *13*, 7790.

(7) Zhang, M.; Zhao, W.; Yang, T.; Gao, R.; Luo, D.; Park, H. W.; Hu, Y.; Yu, A., Vacancy and Growth Modulation of Cobalt Hexacyanoferrate by Porous MXene for Zinc Ion Batteries. *Adv. Energy Mater.* **2024**, 2400543.

(8) Wang, Q.; Li, J.; Jin, H.; Xin, S.; Gao, H., Prussian-blue materials: Revealing new opportunities for rechargeable batteries. *InfoMat* **2022**, *4*, e12311.

(9) Wang, M.; Wang, Q.; Ding, X.; Wang, Y.; Xin, Y.; Singh, P.; Wu, F.; Gao, H., The prospect and challenges of sodium-ion batteries for low-temperature conditions. *Interdiscip. Mater.* **2022**, *1*, 373-395.

(10) He, G.; Nazar, L. F., Crystallite Size Control of Prussian White Analogues for Nonaqueous Potassium-Ion Batteries. *ACS Energy Lett.* **2017**, *2*, 1122-1127.

(11) Hosaka, T.; Fukabori, T.; Kojima, H.; Kubota, K.; Komaba, S., Effect of particle size and anion vacancy on electrochemical potassium ion insertion into potassium manganese hexacyanoferrates. *Chemsuschem* **2021**, *14*, 1166-1175.

(12) Hu, P.; Peng, W. B.; Wang, B.; Xiao, D. D.; Ahuja, U.; Rethore, J.; Aifantis, K. E., Concentration-gradient Prussian blue cathodes for Na-ion batteries. *ACS Energy Lett.* **2020**, *5*, 100-108.

(13) Lee, W.; Yoon, W.-S., Controlling disorder. *Nat. Energy* **2023**, *9*, 10-11.

(14) Cai, Z.; Ouyang, B.; Hau, H.-M.; Chen, T.; Giovine, R.; Koirala, K. P.; Li, L.; Ji, H.; Ha, Y.; Sun, Y.; Huang, J.; Chen, Y.; Wu, V.; Yang, W.; Wang, C.; Clément, R. J.; Lun, Z.; Ceder, G., In situ formed partially disordered phases as earth-abundant Mn-rich cathode materials. *Nat. Energy* **2023**, *9*, 27-36.

(15) Wang, Q.; Yao, Z.; Wang, J.; Guo, H.; Li, C.; Zhou, D.; Bai, X.; Li, H.; Li, B.; Wagemaker, M.; Zhao, C., Chemical short-range disorder in lithium oxide cathodes. *Nature* **2024**, *629*, 341-347.

(16) Liu, H.; Zhu, Z.; Yan, Q.; Yu, S.; He, X.; Chen, Y.; Zhang, R.; Ma, L.; Liu, T.; Li, M.; Lin, R.; Chen, Y.; Li, Y.; Xing, X.; Choi, Y.; Gao, L.; Cho, H. S.-y.; An, K.; Feng, J.; Kostecki, R.; Amine, K.; Wu, T.; Lu, J.; Xin, H. L.; Ong, S. P.; Liu, P., A disordered rock salt anode for fast-charging lithium-ion batteries. *Nature* **2020**, *585*, 63-67.

(17) Xiao, Z.; Meng, J.; Xia, F.; Wu, J.; Liu, F.; Zhang, X.; Xu, L.; Lin, X.; Mai, L., K^+ modulated K^+/vacancy disordered layered oxide for high-rate and high-capacity potassium-ion batteries. *Energ. Environ. Sci.* **2020**, *13*, 3129-3137.

(18) Wei, S.; Chen, S.; Su, X.; Qi, Z.; Wang, C.; Ganguli, B.; Zhang, P.; Zhu, K.; Cao, Y.; He, Q.; Cao, D.; Guo, X.; Wen, W.; Wu, X.; Ajayan, P. M.; Song, L., Manganese buffer induced high-performance disordered MnVO cathodes in zinc batteries. *Energ. Environ. Sci.* **2021**, *14*, 3954-3964.

(19) Ding, J.; Du, Z.; Li, B.; Wang, L.; Wang, S.; Gong, Y.; Yang, S., Unlocking the Potential of Disordered Rocksalts for Aqueous Zinc-Ion Batteries. *Adv. Mater.* **2019**, *31*, 1904369.

(20) Deng, L.; Qu, J.; Niu, X.; Liu, J.; Zhang, J.; Hong, Y.; Feng, M.; Wang, J.; Hu, M.; Zeng, L.; Zhang, Q.; Guo, L.; Zhu, Y., Defect-free potassium manganese hexacyanoferrate cathode material for high-performance potassium-ion batteries. *Nat. Commun.* **2021**, *12*, 2167.

(21) Xue, L.; Li, Y.; Gao, H.; Zhou, W.; Lu, X.; Kaveevivitchai, W.; Manthiram, A.; Goodenough, J. B., Low-cost high-energy potassium cathode. *J. Am. Chem. Soc.* **2017,** *139*, 2164-2167.

(22) Mullaliu, A.; Asenbauer, J.; Aquilanti, G.; Passerini, S.; Giorgetti, M., Highlighting the reversible manganese electroactivity in Na-rich manganese hexacyanoferrate material for Li- and Na-ion storage. *Small Methods* **2020**, *4*, 1900529.

(23) Zhao, C.; Yao, Z.; Zhou, D.; Jiang, L.; Wang, J.; Murzin, V.; Lu, Y.; Bai, X.; Aspuru-Guzik, A.; Chen, L.; Hu, Y. S., Constructing Na-ion cathodes via alkali-site substitution. *Adv. Funct. Mater.* **2020**, *30*, 1910840.

(24) Izatt, R.; Terry, R.; Haymore, B.; Hansen, L.; Dalley, N.; Avondet, A.; Christensen, J., Calorimetric titration study of the interaction of several uni-and bivalent cations with 15-crown-5, 18-crown-6, and two isomers of dicyclohexo-18-crown-6 in aqueous solution at 25. degree. C and. mu.= 0.1. *J. Am. Chem. Soc.* **1976**, *98*, 7620-7626.

(25) Hiland, H.; Ringseth, J. A.; Brun, T. S., Cation-crown ether complex formation in water. II. alkali and alkaline earth cations and 12-Crown-4, 15-Crown-5, and 18-Crown-6 *J. Solution Chem.* **1979**, *8*, 779-792.

(26) Vivier, V.; Orazem, M. E., Impedance analysis of electrochemical systems. *Chem. Rev.* **2022,** *122*, 11131-11168.

(27) Lu, Y.; Zhao, C.-Z.; Huang, J.-Q.; Zhang, Q., The timescale identification decoupling complicated kinetic processes in lithium batteries. *Joule* **2022,** *6*, 1172-1198.